

Image reconstruction from sparse data in synchrotron-radiation-based microtomography

D. Xia,¹ X. Xiao,² J. Bian,³ X. Han,³ E. Y. Sidky,³ F. De Carlo,² and X. Pan³

¹*Institute of Biomedical and Health Engineering and Key Laboratory for Biomedical Informatics and Health Engineering, Shenzhen Institutes of Advanced Technology, Chinese Academy of Sciences, Shenzhen, China*

²*Advanced Photon Source, Argonne National Laboratory, Argonne, Illinois 60439, USA*

³*Department of Radiology, The University of Chicago, Chicago, Illinois 60601, USA*

(Received 24 August 2010; accepted 28 February 2011; published online 18 April 2011)

Synchrotron-radiation-based microcomputed-tomography (SR- μ CT) is a powerful tool for yielding 3D structural information of high spatial and contrast resolution about a specimen preserved in its natural state. A large number of projection views are required currently for yielding SR- μ CT images by use of existing algorithms without significant artifacts. When a wet biological specimen is imaged, synchrotron x-ray radiation from a large number of projection views can result in significant structural deformation within the specimen. A possible approach to reducing imaging time and specimen deformation is to decrease the number of projection views. In the work, using reconstruction algorithms developed recently for medical computed tomography (CT), we investigate and demonstrate image reconstruction from sparse-view data acquired in SR- μ CT. Numerical results of our study suggest that images of practical value can be obtained from data acquired at a number of projection views significantly lower than those used currently in a typical SR- μ CT imaging experiment. © 2011 American Institute of Physics. [doi:10.1063/1.3572263]

I. INTRODUCTION

Micro-CT is a powerful tool for evaluating specimen structures preserved in their natural states, thus preventing structural deformation or destruction encountered otherwise in its histologic fixation and sectioning.¹ Today, both commercial micro-CT systems and synchrotron-radiation-based CT systems can achieve around 1- μ m resolution without x-ray optics,²⁻⁶ and sub-50-nm resolution with x-ray optics.⁶⁻⁹ In terms of microtomography, a third-generation synchrotron radiation source provides partially coherent x-ray beam with enough brilliance to image a millimeter-sized sample at better than 10/micropixel resolution in a few seconds with high sensitivity.¹⁰⁻¹² In comparison to other nondestructive inspection techniques, such as magnetic resonance imaging, conventional micro-CT, and confocal microscopy, synchrotron-radiation-based micro-CT (SR- μ CT) provides the unique capability of performing 3D dynamic studies. In SR- μ CT, a synchrotron source can deliver intense x-rays over a wide energy spectrum, ranging from a few electrovolts to more than a hundred kiloelectrovolts. With a monochromator, x-ray photons within a narrow energy band can be selected for illuminating the imaged specimen virtually free of the beam-hardening effect with optimized contrast sensitivity.

Despite the fact that SR- μ CT possesses unique, desirable properties, such as monochromatic x-ray energy, practical issues exist that limit its applicability to some imaging tasks. One of the issues concerns the large number of projection views that are required currently by existing algorithms such as the filtered-backprojection (FBP) algorithm for yielding images without significant artifacts.¹³⁻¹⁵ Measurements at a large number of projection views not only increase imaging

time but also potentially result in serious radiation damage to the specimen. This is particularly an issue when imaging a living animal *in vivo*. One possible approach to reducing imaging time and radiation damage in SR- μ CT imaging is to decrease the number of projection views, similar to the strategy widely employed in medical imaging.¹⁶ Furthermore, data may be collected only over a limited angular range in some SR- μ CT applications due to certain hardware constraints. For example, in tomographic imaging of specimen *in situ* the specimen is placed in a preserving chamber, which limits the scannable angular range to be less than 180°.

There exist increased interests in developing algorithms for image reconstruction from sparse-view and limited-angular-range data. Inspired by the compressive-sensing work¹⁷⁻¹⁹ on the inverse discrete Fourier transform from its sparse samples, we have recently developed an iterative algorithm for image reconstruction from sparse data in cone-beam computed tomography.^{20,21} The algorithm reconstructs an image through solving a constrained optimization problem in which the image total variation (TV) is minimized subject to data constraints.^{16,20-22} Specifically, the algorithm uses adaptively the steepest descent (ASD) for minimizing the image TV, and uses the projection-onto-convex-sets (POCS) for enforcing data constraints. We thus refer to the algorithm as the ASD-POCS algorithm. In the work, by tailoring the ASD-POCS algorithm to SR- μ CT imaging, we investigate image reconstruction from data acquired at a number of projection views significantly lower than that currently used in a typical SR- μ CT imaging experiment. Also, we investigate image reconstruction from SR- μ CT data collected over an angular range less than 180°.

Report Documentation Page

Form Approved
OMB No. 0704-0188

Public reporting burden for the collection of information is estimated to average 1 hour per response, including the time for reviewing instructions, searching existing data sources, gathering and maintaining the data needed, and completing and reviewing the collection of information. Send comments regarding this burden estimate or any other aspect of this collection of information, including suggestions for reducing this burden, to Washington Headquarters Services, Directorate for Information Operations and Reports, 1215 Jefferson Davis Highway, Suite 1204, Arlington VA 22202-4302. Respondents should be aware that notwithstanding any other provision of law, no person shall be subject to a penalty for failing to comply with a collection of information if it does not display a currently valid OMB control number.

1. REPORT DATE 18 APR 2011		2. REPORT TYPE		3. DATES COVERED 00-00-2011 to 00-00-2011	
4. TITLE AND SUBTITLE Image reconstruction from sparse data in synchrotron-radiation-based microtomography				5a. CONTRACT NUMBER	
				5b. GRANT NUMBER	
				5c. PROGRAM ELEMENT NUMBER	
6. AUTHOR(S)				5d. PROJECT NUMBER	
				5e. TASK NUMBER	
				5f. WORK UNIT NUMBER	
7. PERFORMING ORGANIZATION NAME(S) AND ADDRESS(ES) Argonne National Laboratory, Advanced Photon Source, Argonne, IL, 60439				8. PERFORMING ORGANIZATION REPORT NUMBER	
9. SPONSORING/MONITORING AGENCY NAME(S) AND ADDRESS(ES)				10. SPONSOR/MONITOR'S ACRONYM(S)	
				11. SPONSOR/MONITOR'S REPORT NUMBER(S)	
12. DISTRIBUTION/AVAILABILITY STATEMENT Approved for public release; distribution unlimited					
13. SUPPLEMENTARY NOTES					
14. ABSTRACT					
15. SUBJECT TERMS					
16. SECURITY CLASSIFICATION OF:			17. LIMITATION OF ABSTRACT	18. NUMBER OF PAGES	19a. NAME OF RESPONSIBLE PERSON
a. REPORT unclassified	b. ABSTRACT unclassified	c. THIS PAGE unclassified			

II. MATERIAL AND METHOD

A. SR- μ CT system and imaging experiments

In the work, we used the SR- μ CT system of the Advanced Photon Source at Argonne National Laboratory to collect data from a sample of sea urchin spine (SUS). The SR- μ CT system, as shown in Fig. 1, has seven degrees of motion freedom that allows the control of the rotation-axis orientation and sample position. The detector module is composed of a scintillator, a microscope lens, and a CoolSNAP 2K \times 2K CCD camera (Princeton Instrument, New Jersey) with a pixel size of 7.5 μ m. The scintillator converts an x-ray image into an optical image that is magnified subsequently by the microscope lens and then recorded by the CCD camera. Depending upon the magnification of the microscope lens, the size of a pixel can vary between 0.75 and 6.0 μ m in the image space. The detector is placed on a translation stage that is mounted along the synchrotron-radiation-beam direction so that the sample-to-detector distance can be adjusted.

The SUS sample is composed of highly fenestrated single crystals of high magnesium calcite, and its volume contains about 50% open space. Yet, it has a remarkable strength and flexibility. Because of its unique structural and mechanical properties of high practical interest, SUS is used often as a model system in bionic engineering. The SUS sample used in the work is an *A. radiata* spine with a diameter of 0.6 mm that was collected at Miyako Island, Japan. We used a 2.5 \times Zeiss microscope lens that allows a detector pixel to sample the image space with a resolution of 3.0 μ m. The projection data were acquired at a total of 400 views evenly distributed over 180 $^\circ$ with a 0.45 $^\circ$ angular step. In our experiment, the x-ray energy was 20 keV, and the sample-to-detector distance was 7.0 mm.

B. Imaging model and reconstruction algorithms

1. Imaging model in SR- μ CT

The imaging configuration used in SR- μ CT can be specified by two coordinate systems: the fix-coordinate system $\{x, y, z\}$ and the rotation-coordinate system $\{\xi, \eta, z\}$, which are related, as shown in Fig. 2, through $\xi = x\cos\phi + y\sin\phi$, and $\eta = -x\sin\phi + y\cos\phi$, where ϕ indicates the rotation angle. The detector is assumed to be placed at a distance $\eta = D$, parallel to the (ξ, z) plane. In the well-adapted projection approach in x-ray imaging, the measured x-ray intensity $I^{\eta=D}(\xi, z, \phi)$ at a projection view ϕ can approximately be

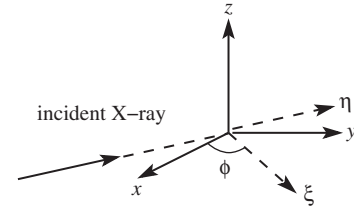


FIG. 2. Illustration of the fixed coordinate system $\{x, y, z\}$ and rotated coordinate system $\{\xi, \eta, z\}$ in the SR- μ CT scan.

expressed as^{23,24}

$$I^{\eta=D}(\xi, z, \phi) = I^{\eta=0}(\xi, z, \phi) \left[1 - D \left(\frac{\partial^2}{\partial \xi^2} + \frac{\partial^2}{\partial z^2} \right) \times \int_{R^2} dx dy (n(x, y, z) - 1) \delta(\xi - x\cos\phi - y\sin\phi) \right], \quad (1)$$

where δ denotes the Dirac delta function, $\mu(x, y, z)$ is the linear attenuation coefficient distribution, $n(x, y, z)$ indicates the real refractive index distribution,

$$I^{\eta=0}(\xi, z, \phi) = I_0 \exp \left[- \int_{R^2} dx dy \mu(x, y, z) \delta(\xi - x\cos\phi - y\sin\phi) \right],$$

and I_0 indicates the intensity of the incident x-ray. The second term in Eq. (1) represents the refraction contribution to measured data. We define

$$g(\xi, z, \phi) = \ln \left[\frac{I_0}{I^{\eta=D}(\xi, z, \phi)} \right] \quad (2)$$

as the projection data in our studies. When the sample-to-detector distance is small such that the refractive contribution is negligible as compared to the first term in Eq. (1), the data function can be modeled adequately as the Radon transform of $\mu(x, y, z)$.²⁵ In contrast, when the sample-to-detector distance is large, a strong contrast enhancement due to the second term in Eq. (1) may be observed around the boundaries between regions with different refractive indices. In this work, the sample-to-detector distance was chosen to be relatively small, and we assume that the data function is the Radon transform of $\mu(x, y, z)$. Therefore, the task of image reconstruction is to determine $\mu(x, y, z)$ from its Radon transform, i.e., the projection data $g(\xi, z, \phi)$.

In actual physical imaging process, other nonlinear factors, i.e., inelastic scattering and small-angle scattering also

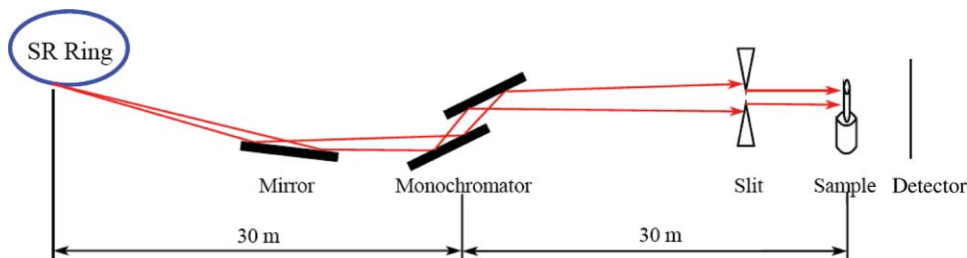


FIG. 1. (Color online) Schematic picture of the SR- μ CT system at beamline 2BM of the Advanced Photon Source at Argonne National Laboratory. The specimen data used in the work were collected with this system.

contribute to the measured x-ray intensity behind the specimen. These contributions may cause data inconsistency with the employed imaging model. Such data inconsistency, however, can be accounted for by the relaxation parameters in ASD-POCS, POCS, and expectation-maximization (EM) algorithms. In FBP algorithm, such data inconsistency has the effect similar to that introduced by noise, which rarely leads to any noticeable error in the reconstructions. In this work, the interest is to compare the performance of different algorithms with real data under different data acquisition conditions. For this purpose, the widely adapted projection model is employed herein.

2. The FBP algorithm

Currently, the FBP algorithm¹⁴ is used most widely for image reconstruction in SR- μ CT. It provides an analytic inversion of the Radon transform and is computationally efficient. When data samples are sufficiently dense, the FBP algorithm can generally yield images of practical usefulness. However, when data are sparsely sampled, it would yield images with significant artifacts. For example, when the number of projection views is limited, as the cases considered in the work, the FBP algorithm yields images with severe streak artifacts. In this work, the FBP results obtained from full data acquired at densely sampled 400 projection views over 180° will be used as reference images, i.e., gold standards, for evaluating the performance of the ASD-POCS algorithm in image reconstruction from data sampled at sparse views or over a limited-angular range. We refer to them as the FBP-reference images.

3. The ASD-POCS algorithm

In this work, we focus on applying the ASD-POCS algorithm to reconstructing images from SUS data acquired at a number of views substantially below what are used currently in SR- μ CT, or over an angular range smaller than 180° . The image reconstruction problem can be expressed as a constrained optimization formulation^{20,21} below:

$$\vec{f}^* = \operatorname{argmin} \|\vec{f}\|_{\text{TV}} \quad \text{s.t.} \quad |M\vec{f} - \vec{g}| \leq \epsilon, \quad (3)$$

where \vec{f}^* denotes the reconstructed image vector that is the solution to the optimization problem, the subscript “TV” is the image TV, matrix M is the linear imaging model, i.e., the Radon transform, and \vec{g} is the projection data vector. Parameter ϵ can be selected for handling potential data inconsistency, including data noise and deviations of the imaging model from the measured data in Eq. (1). In contrast to an unconstrained optimization, the constrained optimization in Eq. (3) allows the incorporation of additional physical constraints such as image positivity and object support. We have recently developed the ASD-POCS algorithm^{20,21} to reconstruct \vec{f}^* by solving the constrained optimization problem in Eq. (3). As mentioned above, the ASD-POCS algorithm iteratively reconstructs the image \vec{f}^* through minimizing the image TV by use of the SD and enforcing the data constraint by use of the POCS. We modify the ASD-POCS algorithm

for its application to image reconstruction from data acquired at sparse views or over a limited angular range.

4. The POCS and EM algorithms

In an attempt to gauge the performance of the ASD-POCS algorithm, in addition to the FBP algorithm, we have also implemented POCS (Ref. 26 and algorithm,^{27,28} and applied them to reconstructing image from the same datasets. Both POCS and EM are widely used iterative algorithms, and they can be interpreted as solutions for their corresponding *unconstrained* optimization problems. Specifically, when data are consistent with the imaging model, the POCS algorithm seeks to minimize the Euclidean distance between the measured and estimated data. On the other hand, the EM algorithm seeks to minimize the Kullback–Liebler divergence between the measured and estimated data. The performance of the POCS and EM algorithms are compared with that of the FBP and ASD-POCS algorithms in the evaluation studies below.

C. Image quality evaluation

We have conducted quantitative performance-evaluation studies of algorithms in image reconstruction from sparse-view data and limited-angular-range data of a SUS specimen acquired with the SR- μ CT. A number of metrics, as summarized below, have been used for quantifying reconstruction quality. It should be pointed out that the metrics can be applied not only to the entire image supports but also to regions of interest (ROI).

The first metric used is the normalized root mean square error (NRMSE), which assesses differences between reconstructed and reference images. It is defined as

$$\text{NRMSE} = \frac{1}{N} \sqrt{\sum_{i=1}^N (f_i - f_i^r)^2} / \left[\frac{1}{N} \sqrt{\sum_{i=1}^N f_i^r{}^2} \right], \quad (4)$$

where f and f^r denote the voxel values in the reconstructed and reference images, and N is the number of voxels within the selected ROI in the image space. In addition to the NRMSE, we have also computed universal quality index (UQI) and mutual information (MI), which are frequently used as quantitative metrics in image processing community for evaluation of image quality.^{29,30} The metric UQI is defined as²⁹

$$\text{UQI}(f, f^r) = \left(\frac{2\mu\mu_r}{\mu^2 + \mu_r^2} \right) \left(\frac{2\text{Cov}(f, f^r)}{\sigma^2 + \sigma_r^2} \right), \quad (5)$$

where $\mu = \frac{1}{N} \sum_{i=1}^N f_i$ and $\mu_r = \frac{1}{N} \sum_{i=1}^N f_i^r$ are the mean values of the reconstructed and reference images, $\sigma = [\frac{1}{N-1} \sum_{i=1}^N (f_i - \mu)^2]^{\frac{1}{2}}$ and $\sigma_r = [\frac{1}{N-1} \sum_{i=1}^N (f_i^r - \mu_r)^2]^{\frac{1}{2}}$ denote the standard deviations of the reconstructed and reference images, and $\text{Cov}(f, f^r) = \frac{1}{N-1} \sum_{i=1}^N \sum_{j=1}^N (f_i - \mu)(f_j^r - \mu_r)$ is the covariance between the reconstructed and reference images. It can be shown that the closer an image to the reference image, the higher the value of UQI. In particular,

UQI reaches 1.0, its maximum value, when the reconstructed image is identical to the reference image.

The metric MI is a quantity that measures the image similarity and can be expressed as³⁰

$$\text{MI}(f; f^r) = \sum_{f_i \in f} \sum_{f_j^r \in f^r} p(f; f^r) \ln \left(\frac{p(f; f^r)}{p(f)p(f^r)} \right), \quad (6)$$

where $p(f)$ and $p(f^r)$ denote the marginal distribution function of the reconstructed and reference images, and $p(f; f^r)$ denotes the joint distribution function of the reconstructed and reference images, and they can be approximated by use of the histograms and joint histograms of reconstructed and reference images. The MI measures the degree of similarity between the histograms of the reconstructed and reference images. The closer the image histogram to the reference-image histogram, the higher the value of MI. In particular, MI achieves the maximum value when the reconstructed image is identical to the reference image.

III. RESULTS

A. Image reconstruction from SR- μ CT data

In our SUS-imaging experiment, the SUS specimen was placed at a distance of $D = 7.0$ mm from the detector, and we then collected the full-dataset, which consists of 256×256 projection images at 400 views evenly distributed over 180° . This dataset is referred to as the full-dataset in our studies. For the imaging configuration under consideration, the refraction contribution to the measured data can be negligibly small because the sample-to-detector distance is small. Therefore, the projection data can be modeled adequately by the 2D Radon transform of the linear attenuation coefficient within the SUS sample.

1. Image reconstruction from the full-dataset

From the full-dataset, we reconstructed an image of the SUS sample using the FBP algorithm, which is shown in Fig. 3(a). This FBP image will be used as the FBP-reference image (i.e., the ‘‘gold standard’’ image) in evaluation studies in Sec. III B because it is currently used in practical SR- μ CT. We also reconstructed an image by use of the ASD-POCS algorithm from the full-dataset, which is shown in Fig. 3(b).

This image will be used as the ASD-POCS-reference image in Sec. III B for the investigation of impact of reference images. Moreover, we used a positivity constraint on pixel values in our reconstructions since the linear attenuation coefficients of the sample are positive. The two images obtained from full-dataset by use of different algorithms appear visually comparable to one another.

2. Image reconstruction from data collected at a reduced number of views

From the full-dataset, we extracted a subset of data at 100 projection views uniformly distributed over 180° to mimic sparse-view data acquisition. From the sparse-view dataset, we used the FBP, EM, POCS, and ASD-POCS algorithms to reconstruct images and display them in the top row of Fig. 4. The FBP-reference image obtained from the full-dataset is displayed in the fifth column of Fig. 4 as the gold standard. Streak artifacts can be observed in the FBP reconstruction obtained from the 100-view projection data, as shown in top panel of the first column of Fig. 4, indicating that the 100-view projection data are under-sampled for analytic reconstruction. In contrast, from the same dataset, the EM, POCS, and ASD-POCS algorithms can yield images with reduced streak artifacts, as shown in the top panels of the second, third, and fourth columns of Fig. 4. Moreover, noise in the image reconstructed by the ASD-POCS algorithm seems to be suppressed as compared to images obtained by use of the EM and POCS algorithms. Overall, the ASD-POCS image is visually more similar to the FBP-reference image than images of other algorithms under study.

In an attempt to investigate the performance of the ASD-POCS algorithm under different angular sampling conditions, we extracted, from the full-dataset, two more subsets of data at 80 and 50 projection views uniformly distributed over 180° . From both datasets, we reconstructed images by use of the FBP, EM, POCS, and ASD-POCS algorithms and display them in the middle and bottom rows of Fig. 4. It can be observed that as the number of projection views decreases, although small structures in the central region of the ASD-POCS reconstruction appear slightly blurred, structures in the peripheral region remain well preserved. In general, the overall image quality reduces, as expected, as the number of projection views decreases. However, it is interesting to notice

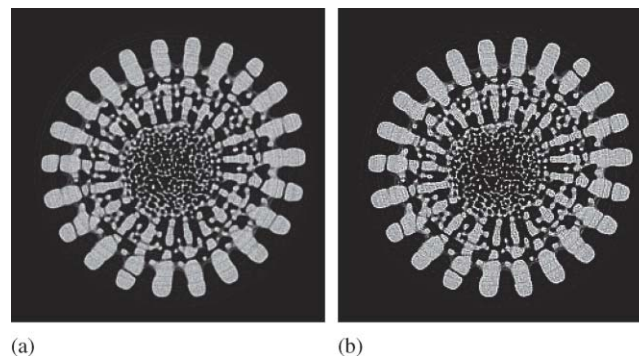


FIG. 3. Image reconstructed from the full data by use of the FBP and ASD-POCS algorithms. Display window: [0.0, 0.5] a.u.

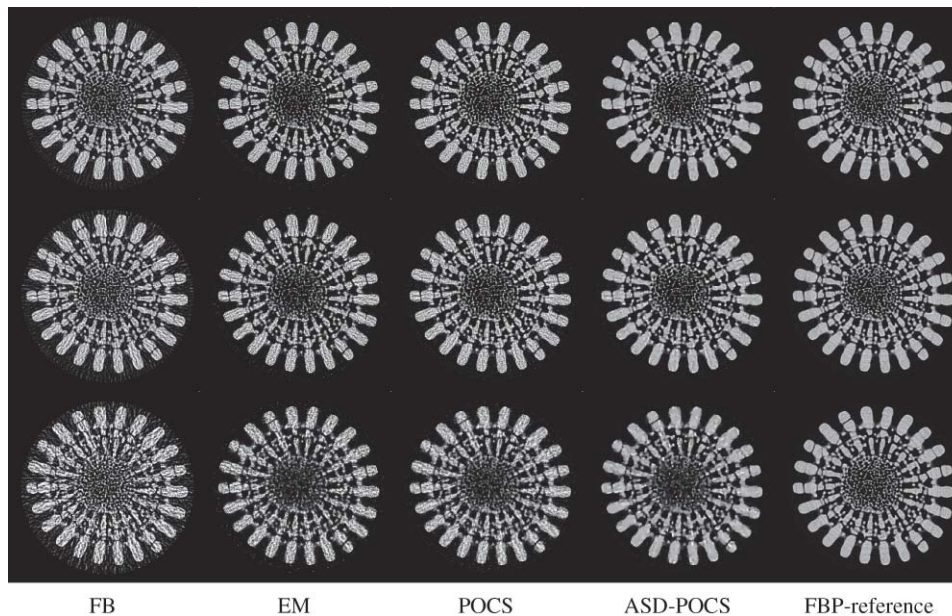


FIG. 4. Images reconstructed from 100-view (top row), 80-view (middle-row), and 50-view (bottom row) full-angular-range data by use of the FBP, EM, POCS, and ASD-POCS algorithms. For comparison, the FBP-reference image is shown in the fifth column. Display window: $[0.0, 0.5]$ a.u.

that, when the number of angular samples is lowered, the quality of iterative reconstructions reduces more slowly than does that of the FBP reconstruction. This observation is particularly true for ASD-POCS reconstructions.

In addition to images within transverse slices shown in Fig. 4, we display 3D reconstructions within selected slices in Fig. 5 obtained from data acquired at 80 views uniformly distributed over 180° . Specifically, we show in the first, second, third, and fourth columns of Fig. 5 images within the coronal slice at $x = 0$ mm and the sagittal slice at $y = 0$ mm, reconstructed by use of the FBP, EM, POCS, and ASD-POCS algorithms, respectively. For comparison, we also show in the fifth column of Fig. 5 FBP-reference images within the corresponding slices. From images within the sagittal and coronal slices, it can be observed that the ASD-POCS algorithm yields images that are visually more similar to the FBP-reference image than those obtained with other algorithms. In particular, the columns of holes within the SUS can readily be identified in both the sparse-view ASD-POCS reconstruction and the

FBP-reference image, whereas they are less well visualized in sparse-view FBP, EM, and POCS reconstructions.

3. Image reconstruction from data collected over a limited angular range

It is not uncommon in SR- μ CT imaging that data may be collected only over a limited angular range^{13,31} because, for example, hardware constraints prevent the system from performing a 180° -scan. In an effort to mimic the limited-angular-range cases, we extracted from the full-dataset three limited-angular-range subsets of data over an angular range of 144° . The three datasets contain 320, 160, and 80 projection views uniformly distributed over 144° . From each of the three datasets, we used the FBP, EM, POCS, and ASD-POCS algorithms to reconstruct images and display the results in Fig. 6. Again, for comparison, we show in the fifth column of Fig. 6 FBP-reference images within the same slice. Significant distortion can be observed in FBP images, resulted

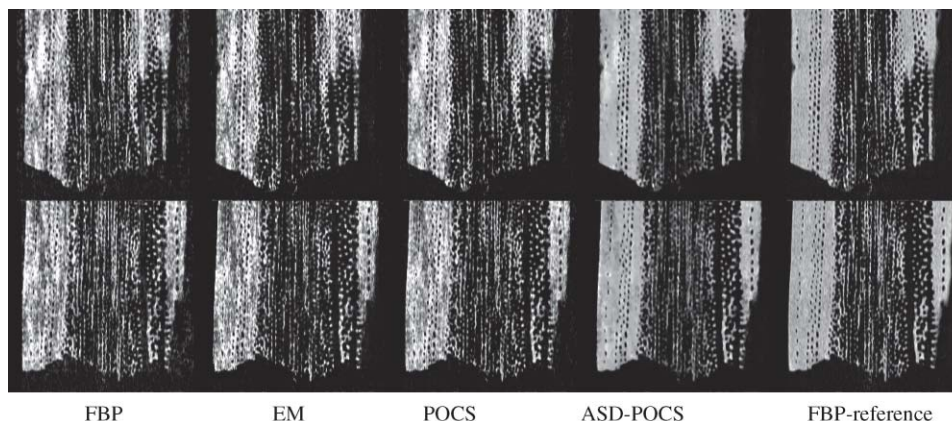


FIG. 5. Images within coronal (upper row) and sagittal (lower row) slices reconstructed from 80-view full-angular-range data by use of the FBP, EM, POCS, and ASD-POCS algorithms. For comparison, the FBP-reference image is shown in the fifth column. Display window: $[0.0, 0.5]$ a.u.

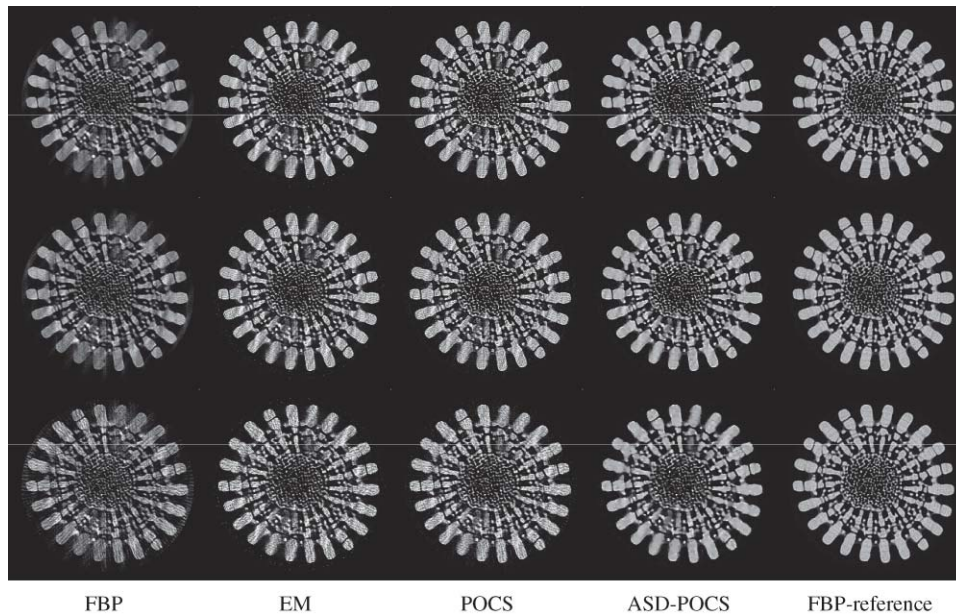


FIG. 6. Images reconstructed from 320-view (top row), 160-view (middle row), and 80-view (bottom row) data acquired over a limited angular range of 144° , by use of the FBP, EM, POCS, and ASD-POCS algorithms, respectively. For comparison, the FBP-reference image is shown in the fifth column. Display window: $[0.0, 0.5]$ a.u.

from the lack of sufficient angular coverage that is required by an analytic reconstruction algorithm. In contrast, some distortion can be identified in images reconstructed by use of the EM and POCS algorithms; whereas the ASD-POCS algorithm yields images with minimum distortion. It is clear that ASD-POCS images are visually more similar to the FBP-reference images than images obtained with other algorithms.

B. Evaluation studies

In addition to the study based upon visual inspection above, we have also carried out evaluation of algorithm performance using quantitative metrics, including NRMSE, UQI, and MI.

1. Quantitative evaluations of image reconstructions

Using images reconstructed from the full-angular-range data containing different numbers of views and the FBP-reference image in Eqs. (4)–(6), we calculated the values of NRMSE, UQI, and MI for FBP, EM, POCS, and ASD-POCS reconstructions and display them in Fig. 7 as functions of view numbers. As the results show, for a given view number, the NRMSE of ASD-POCS reconstruction is generally lower than those of the FBP, EM, and POCS reconstructions, suggesting that the ASD-POCS algorithm yields images that are closer to the FBP-reference image than do other algorithms. As expected, the NRMSE values decrease as the number of views increases, and for 50- and 80-view reconstructions, the NRMSE values of FBP reconstructions are higher than those of EM and POCS reconstructions. However, it is interesting to notice that, for the 100-view case under study, the NRMSEs of FBP reconstructions are actually lower than those of EM and POCS reconstructions. This is because FBP reconstructions

with increased view numbers, i.e., increased angular sampling density, become rapidly similar to the FBP-reference image. Similar observation can be made for the UQI and MI results: the UQIs and MIs of the ASD-POCS reconstructions are generally higher than those of other algorithms under consideration, whereas for 100-view reconstruction, the UQIs and MIs of FBP reconstructions are indeed higher than those of the EM and/or POCS reconstructions.

We have also reconstructed images from data acquired at 320, 160, and 80 views uniformly distributed over 144° . Similarly, using the reconstructed and FBP-reference images in Eqs. (4)–(6), we have calculated NRMSEs, UQIs, and MIs for FBP, EM, POCS, and ASD-POCS reconstructions and display them in Fig. 8. Based upon the results, observations can be made that, for a given view number, NRMSEs of ASD-POCS reconstructions are generally lower than those of the other algorithms, while UQIs and MIs of ASD-POCS reconstructions are higher than those of the other algorithms, which indicate that the ASD-POCS algorithm generally yields images more similar to the FBP-reference image than do the other algorithms under study. It should be noted that the NRMSEs of FBP reconstructions are higher than those of EM and POCS reconstructions. This is different from the cases of image reconstructions from sparse-view data discussed above, revealing the fact that the FBP algorithm is more susceptible to the lack of angular coverage than other algorithms under consideration.

2. Impact of reference images

In our real-data studies, the truth is unknown. As discussed, we used the full-data-FBP reconstruction, i.e., the FBP-reference image, as a surrogate truth, because it is currently used in practical SR- μ CT. Clearly, results of evaluation

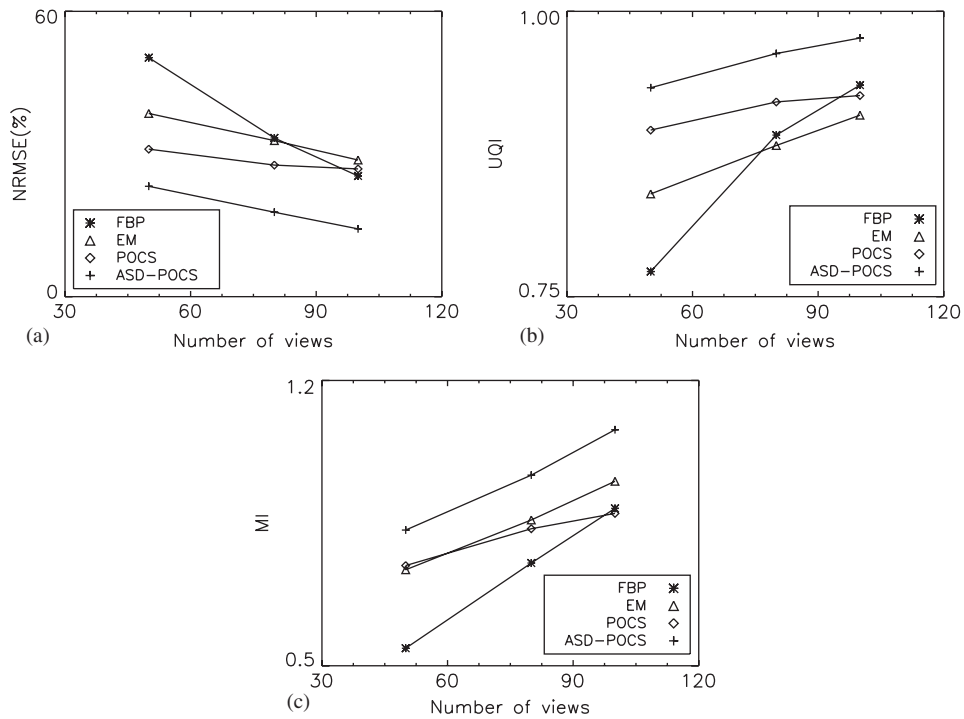


FIG. 7. NRMSEs (a), UQIs (b), and MIs (c) calculated from images displayed in Figs. 4(a)–4(d), which are obtained from the full-angular-range data containing different numbers of views by use of FBP (“*”), EM (“ Δ ”), POCS (“ \diamond ”), and ASD-POCS (“+”) algorithms, with respect to the FBP-reference image.

studies can depend on the selection of reference images. Images from full data reconstructed by use of algorithms other than the FBP algorithm can also be used as reference images. In this case, it is likely that evaluation results differ than those obtained with the FBP-reference image. In an effort to demon-

strate the impact of the selection of reference images on evaluation results, using full-data ASD-POCS reconstruction displayed in Fig. 3(b) as the ASD-POCS-reference image, we repeated the quantitative evaluation study performed in Sec. III B 1 and show some example results in Fig. 9.

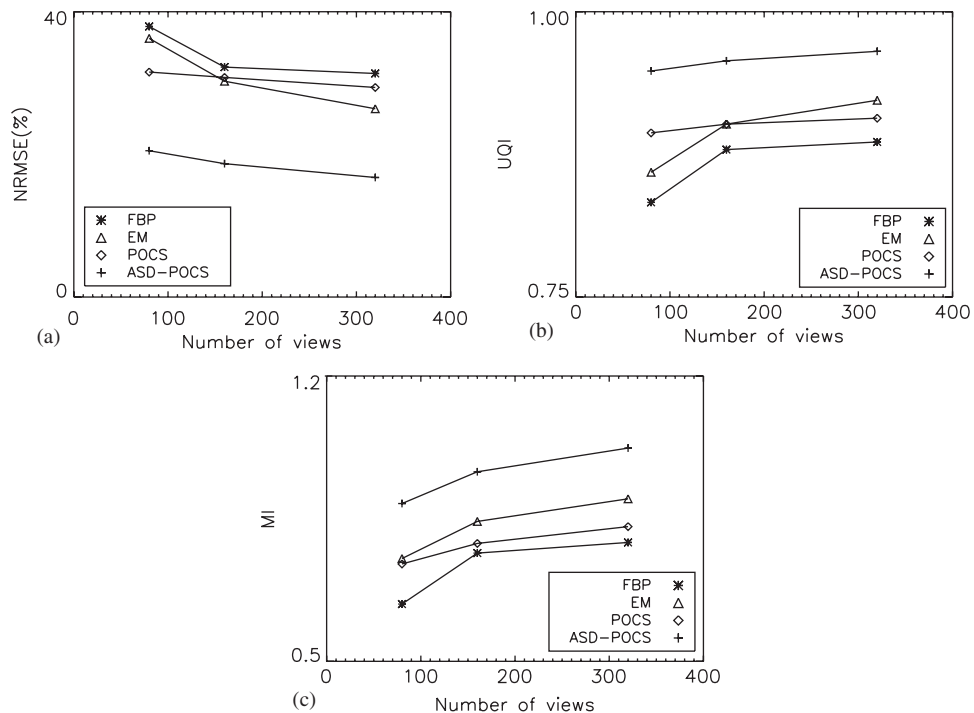


FIG. 8. NRMSEs (a), UQIs (b), and MIs (c) calculated from images displayed in Fig. 6, which are obtained from data containing different number of views acquired over a limited angular range of 144° by use of FBP (“*”), EM (“ Δ ”), POCS (“ \diamond ”), and ASD-POCS (“+”) algorithms, with respect to the FBP-reference image.

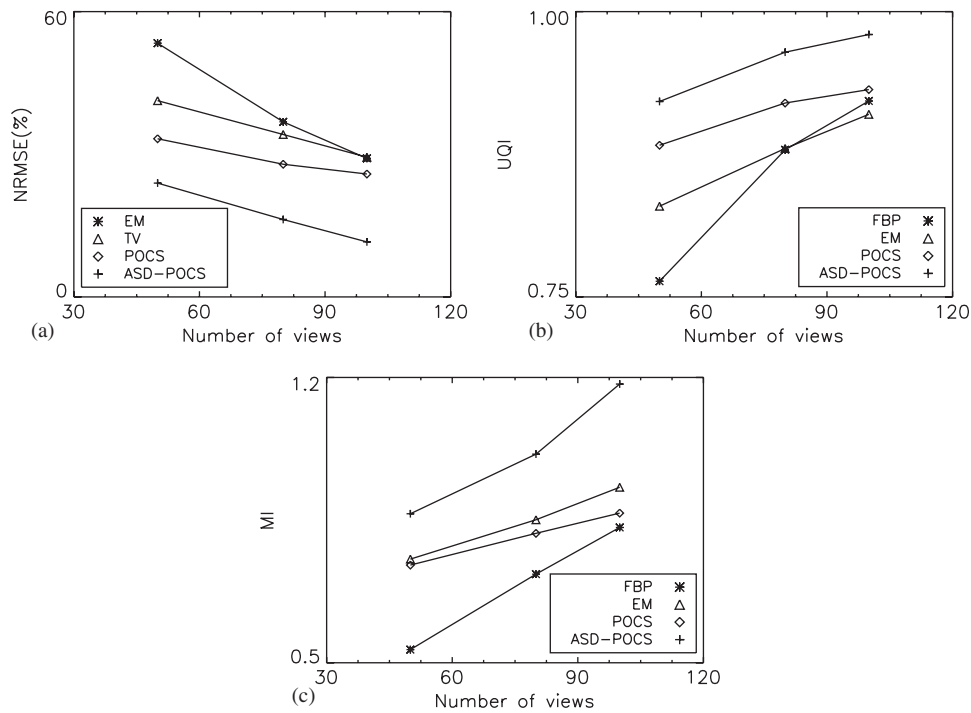


FIG. 9. NRMSEs (a), UQIs (b), and MIs (c) calculated from images displayed in Fig. 4, which are obtained from the full-angular-range data by use of FBP (“*”), EM (“Δ”), POCS (“◇”), and ASD-POCS (“+”) algorithms, with respect to the ASD-POCS-reference image.

Comparison between Figs. 7 and 9 indicates that NRMSEs of the ASD-POCS reconstructions are lowered, while UQIs and MIs of the ASD-POCS are enhanced, suggesting that the use of the ASD-POCS-reference image does lead to evaluation results different from those obtained with the FBP-reference image. Based upon the results in Figs. 8 and 10,

similar observation can also be made for image reconstructions from limited-angular-range data. When either FBP- or ASD-POCS-reference image is used, the ASD-POCS algorithm yields images from sparse-view and/or limited-angular-range data with quality higher than other algorithms under consideration, in terms of the metrics used.

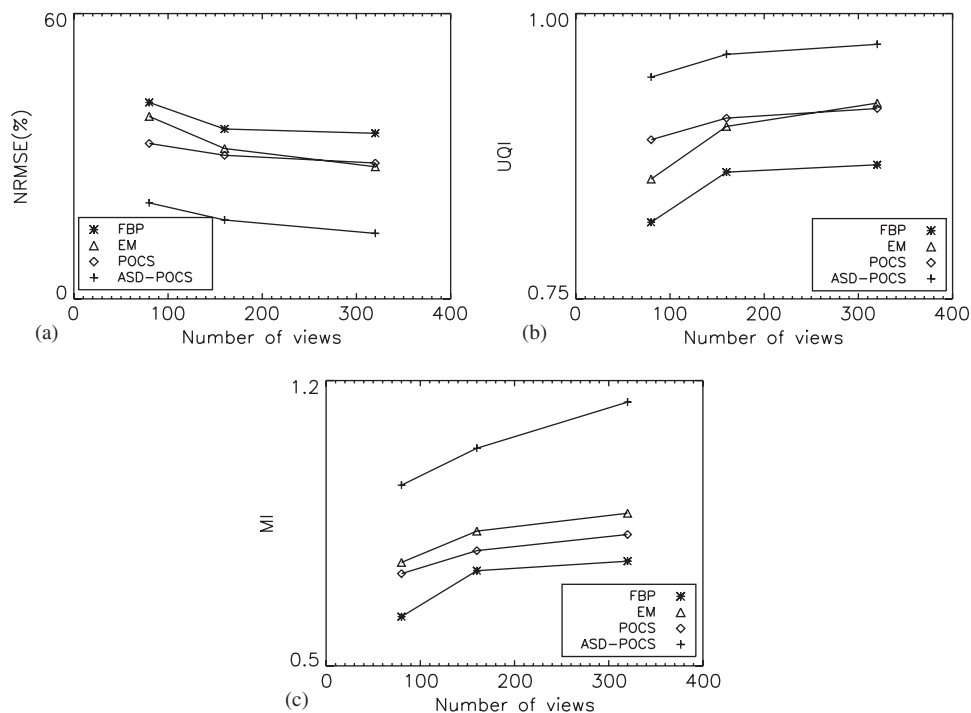


FIG. 10. NRMSEs (a), UQIs (b), and MIs (c) calculated from images displayed in Fig. 6, which are obtained from the data acquired over a limited angular range of 144°, by use of FBP (“*”), EM (“Δ”), POCS (“◇”), and ASD-POCS (“+”) algorithms, with respect to the ASD-POCS-reference image.

IV. CONCLUSIONS

In this work, we have performed image reconstruction from sparse-view data and limited-angular-range data acquired from a SUS sample with SR- μ CT. Results of the study demonstrate that appropriate development of optimization formulation [e.g., Eq. (3)] and the associated algorithms (e.g., the ASD-POCS algorithm) can potentially yield images of practical value for SR- μ CT imaging. The quantitative studies show that, in comparison to the FBP, EM, and POCS algorithms, the ASD-POCS algorithm can yield, from sparse-view and limited-angular-range data, better reconstructions, in terms of NRMSE, MI, and UQI, even when different reference images are used. For the cases under consideration, the ASD-POCS algorithm can reconstruct images with quality comparable to that of the current full-data-FBP reconstructions, from data acquired at considerably fewer views or over a reduced angular range. The work suggests that the ASD-POCS algorithm may allow flexible data acquisition schemes for reducing radiation dose delivered to biologic specimens and thus for minimizing the radiation-induced structural deformation, and that it is also capable of yielding images of practically acceptable quality for limited-angular-range imaging, which is a common situation in tomography experiments *in situ*. It should be noted that other optimization algorithms can be used for replacing the SD and POCS in the ASD-POCS. Therefore, ASD-POCS provides a general iterative approach to solving the constrained optimization problems under study.

ACKNOWLEDGMENTS

This work was supported in part by National Institutes of Health Grant Nos. CA120540 and EB000225. Partial funding for the computation in this work was provided by NIH Grant Nos. S10 RR021039 and P30 CA14599. Use of the Advanced Photon Source at Argonne National Laboratory was supported by the U.S. Department of Energy, Office of Science, Office of Basic Energy Sciences, under Contract No. DE-AC02-06CH11357. J. B. and X. H. were supported in part by DOD Predoctoral Training Grant Nos. BC083239 and PC094510.

¹S. Stock, *Int. Mater. Rev.* **53**, 129 (2008).

- ²T. Weitkamp, P. Tafforeau, E. Bollar, P. Cloetens, J.-P. Valade, P. Bernard, F. Peyrin, W. Ludwig, L. Helfen, and J. Baruchel, *AIP Conf. Proc.* **1234**, 83 (2010).
- ³F. Marone, C. Hintermuller, S. McDonald, R. Abela, G. Mikuljan, A. Isenegger, and M. Stupanoni, *J. Phys.: Conf. Ser.* **186**, 012042 (2009).
- ⁴T. Wilkes, S. Stock, F. De Carlo, X. Xiao, and K. Faber, *Philos. Mag.* **89**(17), 1373 (2009).
- ⁵S. Bugani, M. Camaiti, L. Morselli, E. Van de Castele, and K. Janssens, *X-Ray Spectrom.* **36**(5), 316 (2007).
- ⁶S. Lau, W. Chiu, F. Garzon, H. Chang, A. Tkachuk, M. Feser, and W. Yun, *J. Phys.: Conf. Ser.* **152**, 012059 (2009).
- ⁷G. McDermott, M. A. Le Gros, C. G. Knoechel, M. Uchida, and C. A. Larabel, *Trends Cell Biol.* **19**, 587 (2009).
- ⁸Y. K. Chen, Y. S. Chu, J. Yi, I. McNulty, Q. Shen, P. W. Voorhees, and D. C. Dunand, *Appl. Phys. Lett.* **96**, 043122 (2010).
- ⁹J. C. Andrews, E. Almeida, M. C. H. van der Meulen, J. S. Alwood, C. Lee, Y. Liu, J. Chen, F. Meirer, M. Feser, J. Gelb, J. Rudati, A. Tkachuk, W. Yun, and P. Pianetta, *Microsc. Microanal.* **16**, 327 (2010).
- ¹⁰K. Uesugi, T. Sera, and N. Yagi, *J. Synchrotron Radiat.* **13**, 403 (2006).
- ¹¹A. Momose, W. Yashiro, H. Maikusa, and Y. Takeda, *Opt. Express* **17**, 12540 (2009).
- ¹²N. Limodin, L. Salvo, E. Boller, M. Suery, M. Felberbaum, S. Gailliege, and K. Madi, *Acta Mater.* **57**, 2300 (2009).
- ¹³F. Natterer, *The Mathematics of Computerized Tomography* (Wiley, New York, 1986).
- ¹⁴J. Hsieh, *Computed Tomography: Principles, Design, Artifacts, and Recent Advances* (SPIE Press, Bellingham, WA, 2003).
- ¹⁵X. Pan, E. Y. Sidky, and M. Vannier, *Inv. Prob.* **25**, 123009 (2009).
- ¹⁶J. Bian, J. H. Siewerdsen, X. Han, E. Y. Sidky, J. L. Prince, C. A. Pelizzari, and X. Pan, *Phys. Med. Biol.* **55**, 6575 (2010).
- ¹⁷E. Candes, J. Romberg, and T. Tao, *IEEE Trans. Inf. Theory* **52**, 489 (2004).
- ¹⁸E. Candes and T. Tao, *IEEE Trans. Inf. Theory* **52**, 5406 (2004).
- ¹⁹E. Candes, J. Romberg, and T. Tao, *Comm. Pure Appl. Math.* **59**, 1207 (2005).
- ²⁰E. Y. Sidky, K.-M. Kao, and X. Pan, *J. X-Ray Sci. Technol.* **14**, 119 (2006).
- ²¹E. Y. Sidky and X. Pan, *Phys. Med. Biol.* **53**, 4777 (2008).
- ²²X. Han, J. Bian, D. R. Eaker, T. L. Kline, E. Y. Sidky, E. L. Ritman, and X. Pan, *IEEE Trans. Med. Imaging* **30**, 606 (2011).
- ²³A. Bronnikov, *J. Opt. Soc. Am. A* **19**(3), 472 (2002).
- ²⁴M. Anastasio, D. Shi, F. De Carlo, and X. Pan, *Phys. Med. Biol.* **49**, 121 (2004).
- ²⁵S. Mayo, T. Davis, T. Gureyev, P. Miller, D. Paganin, A. Pogany, A. Stevenson, and S. Wilkins, *Opt. Express* **11**, 2289 (2003).
- ²⁶R. Gordon, R. Bender, and G. T. Herman, *J. Theor. Biol.* **29**, 471 (1970).
- ²⁷A. Dempster, N. Laird, and D. Rubin, *J. R. Stat. Soc. Ser. B (Methodol.)* **39**(1), 1 (1977).
- ²⁸K. Lange and R. Carson, *J. Comput. Assist. Tomogr.* **8**, 306 (1984).
- ²⁹Z. Wang, A. C. Bovik, H. R. Sheikh, and E. P. Simoncelli, *IEEE Trans. Image Process.* **13**, 600 (2004).
- ³⁰F. Maes, A. Collignon, D. Vandermeulen, G. Marchal, and P. Suetens, *IEEE Trans. Med. Imaging* **16**, 187 (1997).
- ³¹A. Louis, *Numer. Math.* **48**, 251 (1986).